The Astrophysical Journal, 895:62 (7pp), 2020 May 20 https://doi.org/10.3847/1538-4357/ab89a4

Planetary Transits at Radio Wavelengths: Secondary Eclipses of Hot Jupiter Extended Atmospheres

Caius L. Selhorst[1], Cassio L. Barbosa[2], Paulo J. A. Simões[3,4], Aline A. Vidotto[5], and Adriana Valio[3]
[1] NAT—Núcleo de Astrofísica, Universidade Cruzeiro do Sul/Universidade Cidade de São Paulo, São Paulo, SP, Brazil; caiuslucius@gmail.com
[2] Dept. de Física, Centro Universitário FEI, São Bernardo do Campo, SP, Brazil
[3] CRAAM, Universidade Presbiteriana Mackenzie, São Paulo, SP 01302-907, Brazil
[4] SUPA School of Physics and Astronomy, University of Glasgow, Glasgow, G12 8QQ, UK
[5] School of Physics, Trinity College Dublin, The University of Dublin, Dublin 2, Ireland
Received 2020 February 18; revised 2020 April 6; accepted 2020 April 14; published 2020 May 26

Abstract

When a planet transits in front of its host star, a fraction of its light is blocked, decreasing the observed flux from the star. The same is expected to occur when observing the stellar radio flux. However, at radio wavelengths, the planet also radiates, depending on its temperature, and thus modifies the transit depths. We explore this scenario simulating the radio lightcurves of transits of hot Jupiters, Kepler-17b, and WASP-12b, around solar-like stars. We calculated the bremsstrahlung radio emission at 17, 100, and 400 GHz originating from the star, considering a solar atmospheric model. The planetary radio emission was calculated modeling the planets in two scenarios: as a blackbody or with a dense and hot extended atmosphere. In both cases the planet radiates and contributes to the total radio flux. For a blackbody planet, the transit depth is in the order of 2%–4% and it is independent of the radio frequency. Hot Jupiters planets with atmospheres appear bigger and brighter in radio, thus having a larger contribution to the total flux of the system. Therefore, the transit depths are larger than in the case of blackbody planets, reaching up to 8% at 17 GHz. Also the transit depth is frequency-dependent. Moreover, the transit caused by the planet passing behind the star is deeper than when the planet transits in front of the star, being as large as 18% at 400 GHz. In all cases, the contribution of the planetary radio emission to the observed flux is evident when the planet transits behind the star.

Unified Astronomy Thesaurus concepts: Eclipses (442); Hot Jupiters (753); Exoplanet atmospheres (487); Radio continuum emission (1340)

1. Introduction

The discovery of exoplanets dates back to 1992, when Wolszczan & Frail (1992) reported the detection of two planets around pulsar PSR B1257+12, by means of precise timing measurements of radio pulses with the Arecibo radio telescope. Currently, the vast majority of the over 4000 exoplanets discovered so far were by the Kepler space telescope mission (Borucki et al. 2010) using the transit method.

The development of the instrumentation to observe planetary transits allowed the improvement of the observations from a tool merely used for the detection of new exoplanets, to a powerful technique for characterizing exoplanets. In the last two decades, it became possible to derive the mass, radius, temperature, and even to probe the physical and chemical components of the atmosphere of a transiting exoplanet (see Fulton et al. 2017; Sánchez-López et al. 2019, for example).

Most of the planetary transits have been observed in the UV-optical-infrared window. Poppenhaeger et al. (2013) reported the observation of a planetary transit of HD 189733b, a hot Jupiter orbiting orbiting a star of spectral type K0V, in soft X-rays. So far, there are only reports of upper limits for possible transits observed at MHz radio wavelengths (Smith et al. 2009; Lecavelier des Etangs et al. 2013). Selhorst et al. (2013) showed the feasibility of detection by simulating observations at 17 GHz of planets, with sizes varying from super-Earth to hot Jupiter, crossing the stellar disk. Observations at radio wavelengths were restricted to the interaction between the parent star and the atmosphere of the exoplanet (see for example Pope et al. 2019, and references therein). As Selhorst et al. (2013) showed, the observation of planetary transits at radio wavelengths is a very promising tool, especially for magnetically active stars such as red dwarfs.

In this paper, we explore the high-frequency radio regime, which is accessible with the Karl G. Jansky Very Large Array (JVLA) and Atacama Large Millimeter/submillimeter Array (ALMA). We note that exoplanets have also been predicted to produce auroral emission in the low-frequency radio regime (Farrell et al. 1999; Grießmeier et al. 2007; Vidotto et al. 2010b, 2019). The exoplanetary auroral emission, generated by electron cyclotron maser instabilities (ECMI), is believed to arise from the interaction between the magnetized stellar wind and the planet magnetic field, which would enhance the detectability of exoplanets. Such an emission would make the planet brighter than the stellar emission itself at lower frequencies (e.g., Farrell et al. 1999; Vidotto et al. 2015).

This emission is believed to be similar to auroral emission observed in brown dwarfs (Kao et al. 2016) and M dwarfs (Hallinan et al. 2009; Llama et al. 2018). In the exoplanetary case, however, the frequency of emission is expected to be much lower, due to lower magnetic field strengths. For this reason, radio arrays such as LOFAR and, in the future Square Kilometre Array (SKA; Dewdney et al. 2009), are better suited to observe exoplanetary auroral emission (Zarka et al. 2015).

There have been numerous unsuccessful attempts to observe exoplanetary radio emission at lower frequencies (e.g., Lazio & Farrell 2007; Smith et al. 2009; Hallinan et al. 2013; Sirothia et al. 2014) A possible, but yet unlikely, reason for this is that hot Jupiters are unmagnetized and thus they do not generate ECMI. Alternatively, the non-detections are due to observations not being sufficiently sensitive, or that they are conducted

at frequencies that do not match the (cyclotron) frequency of emission (Bastian et al. 2000). Other possibilities are that a dense planetary atmosphere (Weber et al. 2017) or a dense stellar wind (Vidotto & Donati 2017; Kavanagh et al. 2019) could suppress ECMI planetary emission. The stellar wind itself can absorb planetary radio emission, causing radio planets to be eclipsed by the wind of their host stars (Kavanagh & Vidotto 2020). While, like us, these authors computed radio eclipses of exoplanets, Kavanagh & Vidotto (2020) did not discuss eclipses due to thermal emission from the planet. Here, on the other hand, we focus on radio transits and eclipses that are caused by thermal emission of the planet. The advantage of our study is that, contrary to ECMI studies, we do not need to prescribe an unknown planetary magnetic field strength to predict the frequency of the emission. Given the large frequencies we investigate here, planetary magnetic fields would need to be unreasonably high (>6 kG) to cause ECMI at such high frequencies.

Recently, Vedantham et al. (2020) reported LOFAR detection of low-frequency radio emission from the quite M dwarf GJ 1151, believed to be induced by a close-in terrestrial mass planet (Pope et al. 2020). Investigation of radio emission of exoplanets, from low to high radio frequencies, is thus very timely. The effects of the interaction of the stellar emission with the dense and hot atmosphere of close planets at radio wavelengths are explored in this work.

Primary and secondary transit simulations are performed at three distinct radio frequencies, 17, 100, and 400 GHz, generated by bremsstrahlung emission.

We report the radio lightcurves produced by our simulations for such a planet transit in the next section, whereas the discussion and conclusions are presented in the following sections.

2. Simulations

The lightcurve at radio wavelengths of a solar-like star is calculated assuming that the radio emission is similar to that observed for the Sun (Liseau et al. 2016). In this case, the radio emission of the host star was estimated using the solar atmospheric model proposed by Selhorst et al. (2005a; hereafter referred to as the SSC model). The SSC model was chosen due to the very good agreement with the solar brightness temperature observed at various radio frequencies (1–405 GHz), as well as its good agreement with the limb brightening observed in solar maps obtained at 17, 100, and 230 GHz (Selhorst et al. 2005a, 2005b, 2019).

The transit simulations were made based on a model developed in Silva (2003) where the 2D images of the star (with limb brightening in this case) and that of the planet (opaque or not) are created. The position of the planet in its orbit is calculated at a given time interval and the sum of all the pixels in the image of the star–planet systems composes the lightcurve.

While in Selhorst et al. (2013), the transiting planet was taken as an opaque disk, in this work, two scenarios are considered to estimate the hot Jupiter radio contribution. In the first one, the orbiting planet is assumed to behave as a blackbody (BB) without an atmosphere, which means that the planet's brightness and effective temperatures are the same ($T_{\rm Bp} = T_{\rm eff}$). Following the results obtained for planetary transits observed at X-rays (Poppenhaeger et al. 2013), the second scenario considers a planetary dense and hot atmosphere, which increases the planet size at radio wavelengths. Both approaches are described in more detail bellow.

2.1. Stellar Maps

As mentioned above, the parent star was considered to be solar-like, thus the brightness temperature was calculated using the SSC atmospheric model. For simplicity, bremsstrahlung was considered to be the unique emission mechanism, where we neglected the gyro-resonance contribution and the refraction effects (see Tan et al. 2015) to the quiet Sun brightness temperature ($T_{\rm BS}$) at radio frequencies greater than ~5 GHz.

The brightness temperature of the stellar disk was calculated from spatially resolved solar observations at three radio frequencies: 17, 100, and 400 GHz. The emission at each frequency is formed at different atmospheric layers, with the higher frequencies originating closer to the photosphere. The brightness temperature for each frequency presents distinct values at the disk center and their images also display different limb brightening intensities.

The center-to-limb variation of the brightness temperature at 17, 100, and 400 GHz is shown in Figure 1 (green, blue, and magenta curves, respectively). While the 17 GHz emission originates from the upper chromosphere and presents a brightness temperature raging from 10×10^3 K at disk center to a maximum of 16×10^3 K at the limb, the emission observed at 100 and 400 GHz is produced in the atmospheric region close to the temperature minimum region, i.e., the region between the photosphere and chromosphere, resulting in smaller temperatures, from 7.2×10^3 to 9.5×10^3 K at 100 GHz and from 5.3×10^3 to 7×10^3 K at 400 GHz. These center-to-limb profiles were used to generate bidimensional stellar maps. Each map was made with the same angular size of the Sun at 1 au, with 3″ pixel resolution (see Figure 2(a)). This spatial resolution smoothed the limb brightening profiles. As a result, the position of the maximum value of the brightness temperature is the same at 17 and 100 GHz, 963″, whereas the limb maximum brightness temperature at 400 GHz occurs at 960″.

2.2. BB Planet

While in the radio simulations performed by Selhorst et al. (2013) the planets eclipsing the star were considered as opaque disks, in our first approach in this work, the planets were simulated as BB objects without an extended atmosphere. Therefore, the planet brightness and effective temperatures are equal ($T_{\rm Bp} = T_{\rm eff}$). We simulated the transit of two hot Jupiter planets, Kepler-17b and WASP-12b. Even though both planets orbit G-type stars, they present distinct sizes and temperatures. The planets parameters such as size, temperature, orbital period, and semimajor axis were obtained from the Extrasolar Planet Encyclopedia (www.exoplanet.eu) and are listed on Table 1.

Both planets orbit very close to their host star, limiting the prospects of spatially resolving the system by future radio observations. Thus, the observed flux would be the total flux of the stellar system $F_{\rm total} = F_S + F_p$, where F_S and F_p are, respectively, the star and the planet radio fluxes. During the transit of the planet in front of the star, a reduction of the total flux is expected due to the partial blockage of the stellar flux by

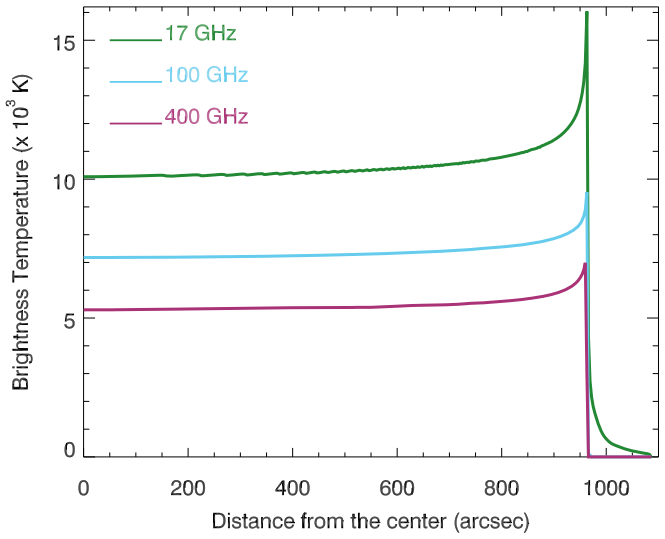

Figure 1. Center-to-limb variation of the stellar brightness temperature at 17, 100, and 400 GHz, plotted in green, blue, and magenta, respectively.

the planet. In this case, the observed flux (F) is calculated as

$$F = \frac{F_{\rm total} - F_{\rm abs}}{F_{\rm total}},$$

where $F_{\rm abs}$ is the stellar radio flux blocked by planet.

An example of the stellar disk and the transiting planet is shown in Figure 2(a) for WASP-12b at 400 GHz, where the dashed line represents the path of the planet. The resulting radio lightcurves are shown in Figure 2(b) for two cases: the transit of the planet in front (green curve) and behind the star (magenta curve). Since the planets were simulated with uniform temperatures, when the planet hides behind the star, the lightcurves have flat intensities, as can be seen by the magenta curve in Figure 2(b). This behavior contrasts with the intensity variation in the lightcurve during the planetary transit in front of the star (green curve), which presents a larger reduction at the edges caused by the planet blocking the limb brightening of the star, which is shown in detail in the right side boxes.

The flux reduction caused by the blockage of the limb brightening should be observed by the first and last points of the transit in which the planet is completely in front of the stellar disk (Figure 2(a)). These transit positions are shown by dotted vertical lines in Figures 2(b) and (d). Due to the stellar limb brightening, the strongest flux reduction during the transit occurs when the planet is near the limb of the star. Note that for optical transits, the effect is opposite: due to limb darkening the strongest flux reduction happens during the center of the transit. In the cases of transits with large impact parameters, the transit duration would be shorter and thus its detection would require observations with short cadence.

Transit simulations were performed for the two planets, where the radio flux reduction of the transit lightcurve in each case was estimated at the frequencies of 17, 100, and 400 GHz. These flux reductions during transits reflect the planet contribution to the star–planet system flux. For each case, the results are listed in the last six columns of Table 2. The transit simulation of the two planets showed a decrease in flux of less than 1.7% for Kepler-17b, and less than 3.6% for WASP-12b, which has a larger radius than Kepler-17b. As expected, the larger and hotter planet, WASP-12b, caused a larger flux reduction than that generated by Kepler-17b. In the case of the transit lightcurve of Kepler-17b obtained considering the planet BB temperature, the decrease in flux of about 2% is almost equal to that obtained with the earlier simulation done by Selhorst et al. (2013) considering opaque planets.

The simulations also showed that the primary transit depth does not vary with frequency (see Table 2). On the other hand, the simulation of the secondary eclipse, when there is no contribution from the planet to the total flux, showed that the relative transit depth reduces with frequency, from 17 to 400 GHz, implying that the relative contribution of the planet radio emission to the total radio flux increases with frequency.

2.3. Hot Jupiter Atmosphere

To simulate the influence of hot Jupiter atmospheres in transit observations at radio frequencies, we considered a spherically symmetric atmospheric model, similar to the one proposed by Poppenhaeger et al. (2013). Here, the atmosphere was considered fully ionized at the region where the radio emission is formed, with an electron density of $n_e = 7 \times 10^9$ cm^{-3} at 1.0 $R_{\rm J}$ above the visible disk of the planet, that is 10 times smaller than the used by Pope et al. (2019) in their estimations. The density scale height was kept equal to that one used in Pope et al. (2019), that is $H = 5000$ km. For simplicity, the temperature of the atmosphere was assumed to be constant, with a value of $T = 15{,}000$ K, at the region in which the radio emission is formed.

In our adopted atmospheric model the planetary atmosphere becomes optically thick at the selected radio frequencies. The bremsstrahlung opacity, κ_ν, for a fully ionized plasma is proportional to $n_e^2 \nu^{-3}$. As a consequence, the optical depth ($\tau_\nu = \int \kappa_\nu ds$) reaches values greater than unity at distinct atmospheric altitudes for the simulated radio frequencies. Although this makes the planet appear larger at lower radio frequencies, as shown in Table 2, the difference between the smallest (400 GHz) and the biggest (17 GHz) radio planet is only 0.03 $R_{\rm S}$, where $R_{\rm S}$ is the stellar radius, for both Kepler-17b and WASP-12b. Therefore, our modeled radio emission from the planets corresponds to a 15,000 K homogeneous brightness temperature.

Once the model for the radio emission from the hot Jupiter planets was developed, we calculated the transit lightcurves. Figure 2(c) shows the transit of the hot WASP-12 planet and the star at 400 GHz. In this scenario, except for the sharpest edge of the limb brightening at 17 GHz (see Figure 1), the brightness temperature of the planet is larger than the brightness temperature of the star. Thus, the contribution of the planet to the total radio flux is larger than that in the BB case. This is due to the inclusion of the atmosphere, resulting in a higher brightness temperature and larger size of the planet. This effect can be seen in the larger transit depth obtained in the simulations for both Kepler-17b and WASP-12b planets. The lightcurves of the transit of the hot Jupiter in front of the star (green) and behind it (magenta) are depicted in Figure 2(d) for WASP-12b at 400 GHz.

The transit depth obtained from the simulations are listed on the bottom two rows of Table 2 for transits of the planets in front of and behind the star. Due to the similar planet sizes in radio, the planet's contribution to the total flux F rises with frequency, since $F \propto \nu^2$. The flux reduction due the planetary

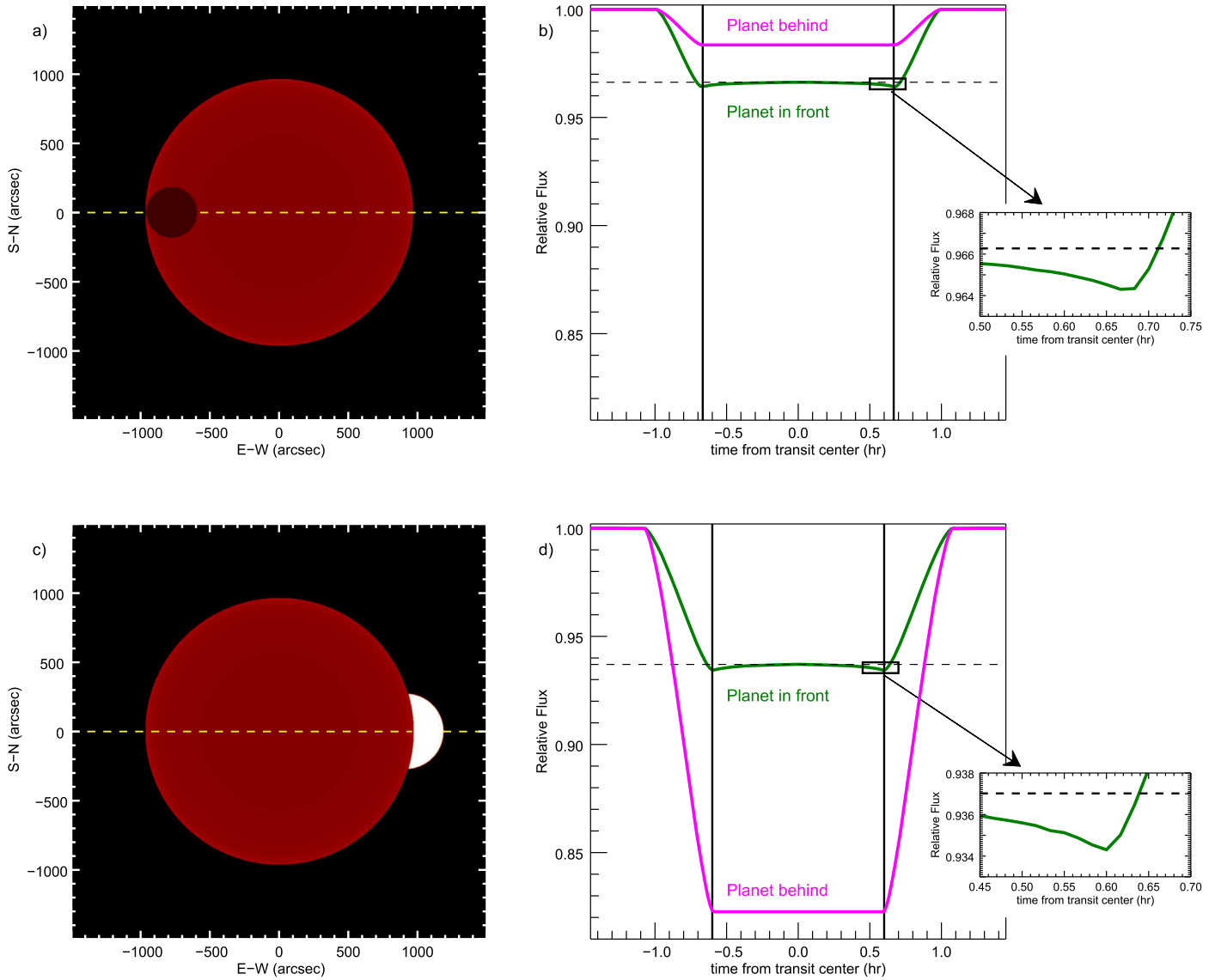

Figure 2. (a) Stellar map simulated at 400 GHz, eclipsed by a planet with WASP-12b characteristics. The dashed line represents the path of the planet. (b) 400 GHz lightcurves obtained caused by the transit of the planet in front (green) and behind (magenta) the star. The dashed line is the flux reduction at the center of the transit, while the limb reduction bellow this value is shown in details in the right side box. The vertical dotted lines were placed at the deepest transit positions. (c) Stellar map simulated at 400 GHz eclipsing a planet with WASP-12b characteristics and with a hot and dense atmosphere. (d) 400 GHz lightcurves obtained by the transit of the planet in front (green) and behind (magenta) the star.

Table 1
Characteristics of the Planets Used in the Simulations

Planet	Radius (R_S)	T_{eff} (K)	Orbital Period (days)	Semimajor Axis (au)
Kepler-17b	0.13	1655	1.4857	0.0259
WASP-12b	0.19	2593	1.0914	0.0234

transits presented distinct behaviors if the planet is in front or behind the star.

When the planet transits in front of the star, the transit depth is larger at lower frequencies (Table 2 columns 6–8), which is caused by the larger contribution of the stellar emission to the total flux (Figure 3). For Kepler-17b, the transit depth varies from 5.6% to 4.4% from 17 to 400 GHz, whereas this variation is larger for WASP-12b, the depth decreases from 8% to 6.6% from 17 to 400 GHz.

On the other hand, when the planet passes behind the star, the transit becomes deeper with increasing frequency (Table 2), reaching a flux reduction of 18% at 400 GHz for WASP-12b. Moreover, because the brightness temperature of the planet is greater than that of the star, in all simulations with a hot planetary atmosphere, the transit is deeper when the planet passes behind the star (see Figure 2(d)).

For all frequencies simulated here, the hot Jupiters secondary transits were deeper than the primary ones. However, the differences between them reduces with decreasing frequency, while at 400 GHz the transit depth of WASP-12b varies from a primary transit with 6.6% maximum reduction to a secondary with 17.7% reduction, at 17 GHz the depth changed from 8.1% to 11.5%, for the primary and secondary transits, respectively. Moreover, assuming the models used in the simulations, the primary transit should became deeper than the secondary one when the stellar brightness temperature becomes equal to the hot Jupiter one, which is obtained around 5 GHz in the SSC

Table 2
Flux Reduction due to Transits of Blackbody and Hot Jupiter Planets

Planet	T_{Bp} (K)	Radius in Radio (R_S)			Largest Flux Reduction					
					Planet in Front of the Star			Planet Behind the Star		
		17 GHz	100 GHz	400 GHz	17 GHz	100 GHz	400 GHz	17 GHz	100 GHz	400 GHz
Blackbody planets										
Kepler-17b	1655	0.13	0.13	0.13	1.7%	1.7%	1.7%	0.3%	0.4%	0.5%
WASP-12b	2593	0.19	0.19	0.19	3.6%	3.6%	3.6%	0.8%	1.2%	1.6%
Hot Jupiter atmosphere										
Kepler-17b	15000	0.25	0.23	0.22	5.6%	4.9%	4.5%	7.8%	9.8%	11.9%
WASP-12b	15000	0.31	0.30	0.28	8.1%	7.4%	6.6%	11.5%	14.8%	17.7%

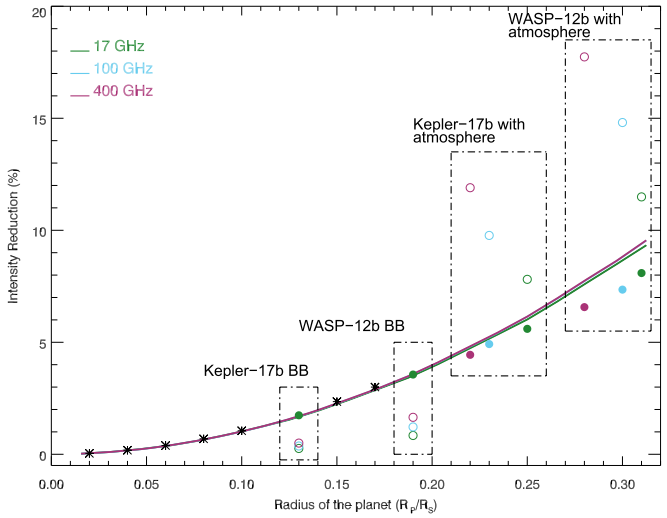

Figure 3. Transit depth of planets with different sizes at three distinct frequencies 17, 100, and 400 GHz, shown in green, blue, and magenta, respectively. Following Selhorst et al. (2013), the solid lines were obtained with the transit of opaque planets. The asterisks represent the results obtained by Selhorst et al. (2013) for different size planets. The results obtained for the BB planet model, and planets with an extended hot atmosphere (Table 2) are shown as circles, in which the filled circles represent the primary transit, whereas the open circles depict the secondary eclipse.

model (see Figure 3 in Selhorst et al. 2005a). Furthermore, for lower frequencies typically formed at coronal heights, the primary transits tend to be much deeper than the secondary ones.

3. Discussion

To verify the consistency of the synthetic maps, the quiet star simulations performed by Selhorst et al. (2013) using the 17 GHz maps observed by the Nobeyama Radioheliograph were reproduced here with the synthetic maps instead of the observed ones. In these simulations, the planet was considered as an opaque disk. Figure 3 shows the relative flux reduction during transits with planet size for three frequencies (17, 100, and 400 GHz). The solid lines represent the simulations performed with the synthetic stellar maps based on the SSC model and the asterisks are the results obtained by Selhorst et al. (2013) using an observed quiet Sun map. In these simulations, the differences between results obtained at 17 GHz (green) and higher frequencies are very small. Moreover, the results obtained at 100 (blue) and 400 GHz (magenta) lines are almost the same and cannot be distinguished in the plot.

For comparison, the results obtained in this work are also plotted in Figure 3 for Kepler-17b and WASP-12b. Both models of the BB planet and that with a hot extended atmosphere are shown in the rectangular boxes. The transit depths during primary transits (filled circles) and secondary eclipses (open circles) for the three radio frequencies 17 (green), 100 (blue), and 400 GHz (magenta) are plotted.

Clearly seen is the larger depth for the secondary eclipse compared to that of the primary transit, and how it increases for larger radio frequencies. As expected, the lightcurve intensity reduction is also larger for the hot extended planetary atmosphere because of the bigger size and flux contribution due to larger temperature.

In this paper, we suggest that the puffy atmospheres of close-in giant planets can be revealed in secondary transits in high-frequency radio observations. Close-in exoplanets receive a large flux of energetic radiation from their host stars. In particular, the EUV and X-ray photons can photoionize hydrogen-dominated atmospheres, which are heated to temperatures that can reach above 10,000 K. As a consequence, these atmospheres expand and more easily evaporate. Planetary evaporation has been observed in several close-in planets in Lyα transits (e.g., Vidal-Madjar et al. 2003; Kulow et al. 2014; Bourrier et al. 2016) and, more recently, are being revealed in the near-infrared He I triplet at 10833 Å (Nortmann et al. 2018; Spake et al. 2018; Allart et al. 2019). Evaporation rates are higher in close-in planets that orbit active stars (Johnstone et al. 2015; Kubyshkina et al. 2018; Allan & Vidotto 2019; Oklopčić 2019) due to their higher EUV and X-ray luminosities. Indirect evidence of atmospheric evaporation in close-in planets has also been seen in the distribution of planetary radii (Beaugé & Nesvorný 2013; Mazeh et al. 2016; Fulton et al. 2017).

Here, we focus on the case of eclipsing planets that have spherically symmetric, dense, and hot atmospheres. We note however that there is increased evidence both from observations (Fossati et al. 2010; Ehrenreich et al. 2015) as well as from models (Villarreal D'Angelo et al. 2014, 2018; Matsakos et al. 2015) that this is not always the case. Interactions with stellar winds and orbital motion predict that atmospheric material should be distributed asymmetrically around the planet, causing accretion streams, bow shocks, and comet-like tails (e.g., Lai et al. 2010; Vidotto et al. 2010a; Bourrier & Lecavelier des Etangs 2013). We leave the effects that

asymmetric atmospheres have on radio lightcurves to a future study.

Our calculations assumed that planetary atmospheres do not vary in relatively short timescales. However, temporal variations in stellar activity are expected to lead to transit variability in timescales as short as a few transits apart up to stellar cycle timescales (Vidotto et al. 2011; Llama & Shkolnik 2015). Indeed, Lecavelier des Etangs et al. (2012) reported variations in the Lyα transits of HD 189733b separated by 1.5 yr. The transit variabilities were interpreted as being caused either by changes in stellar wind conditions or by the observed stellar flare, which could have increased high-energy irradiation and thus caused stronger evaporation. One way to overcome the impact of stellar variability in the interpretation of transit signals is by combining data from multiple transits (Llama & Shkolnik 2016).

We investigated the possibility of the detection of radio transits using current state-of-the-art and future radio telescopes, for the conditions simulated in this work. For 17 GHz, we used the curves of the sensitivity of future radio telescopes (Figure 1 of Pope et al. 2019) as a guide. Considering a solar-type star, like ϵ Eri at its true distance (3.2 pc) and a flux reduction of 10% during the transit, the transit would be barely detectable after 1 hr of integration time at JVLA. With the SKA1 telescope it would be possible to observe transits at a 5 minutes cadence, which would allow the detection of the progression of the transit itself. At a distance of 20 pc, the 10% transit for the same solar-type star would only be detected by the planned SKA2 extension, but only after more than 30 minutes of integration time.

For higher frequencies, we used the sensitivity calculator to estimate the detection of a 10% transit of such solar-type star. In this case, we used the same input parameters of Selhorst et al. (2013): flux of 340 μJy at 345 GHz with bandwidth of 16 GHz and optimal observing conditions for 50 12 m antennas. To be able to detect the transit, the rms of the observation has to be within at least at 10% of the flux, which means 34 μJy. This could be achieved in less than 8 minutes of integration time, possibly allowing the detection of the shape of the transit curve.

4. Conclusions

In this work, we estimated the planet radio flux contribution relative to that of the star taking into consideration the planet atmosphere at three radio frequencies of 17, 100, and 400 GHz. Two models were analyzed, a BB planet and a planet with an extended atmosphere with a brightness temperature of 15,000 K. The planetary flux contribution was estimated measuring the transit depth during the secondary eclipse.

Simulations of the lightcurve during the primary and secondary transits of hot Jupiters around solar-type stars at radio frequencies were made. The star was simulated with the solar atmospheric model SSC (Selhorst et al. 2005a) at 17, 100, and 400 GHz. The physical characteristics of Kepler-17b and WASP-12b were used in the simulations, where the two atmospheric scenarios were considered. In the first one, the planets were considered as BBs, which implies that the planet brightness and effective temperatures were equal, moreover, the radio planet had the same size as observed at optical wavelengths.

Since future radio observations will detect the whole stellar system (star+planet), the BB planet contribution is low, causing a decrease of <4% in the total flux during transits. This result is similar to that obtained by Selhorst et al. (2013) for opaque planets. However, the consideration of the planet temperature (about 1650 K and 2600 K for Kepler-17b and WASP-12b, respectively) resulted in a secondary transit reflecting the planet larger contribution to the total radio flux (see Table 2).

In the second approach, the effect of the planetary extended atmosphere was simulated using the characteristics proposed by Poppenhaeger et al. (2013) to reproduce the X-rays transit profiles. The hot and dense planetary atmosphere increases the size of Kepler-17b from 0.13 R_S to 0.22–0.25 R_S, whereas, WASP-12b grew from 0.19 R_S to 0.28–0.31 R_S. In both cases, the smallest and largest sizes where obtained at 400 and 17 GHz, respectively. Due to the radio planet increase, the primary transit became deeper, with a depth varying from 5.6% to 4.4% from 17 to 400 GHz for Kepler-17b, whereas for WASP-12b, the depth decreased from 8% to 6.6% from 17 to 400 GHz.

Since the atmosphere is dense enough to became optically thick and the plasma temperature was 15,000 K, the planet brightness temperature is greater than that expected for the star at the simulated frequencies. Nevertheless, due to the larger star size, the stellar flux is still greater than the planetary one. However, the radio planet contribution to the system total flux increased considerably reaching approximately 8%–12% for Kepler-17b and 11%–18% for WASP-12b, increasing in frequency from 17 to 400 GHz. The radio planet contribution could be obtained by the deep flux reduction during the planet secondary transit, i.e., when the planet is totally eclipsed by the star.

While Pope et al. (2019) studied the possibility of a planetary transit to be observed at low radio frequencies by the SKA, here we presented an analysis at higher frequencies (17, 100, and 400 GHz), which could be currently observed by the JVLA and ALMA. In comparison with Selhorst et al. (2013), the inclusion of a planetary atmosphere increased the possibility of primary planetary transit be observed at radio frequencies due to the increase of the planet radius. Moreover, our results showed new observational possibilities to verify the planetary flux through secondary transits, which is a promising tool in the millimeter and submillimeter range.

The authors wish to thank the anonymous referee for their comments and suggestions that improved the revised version of the paper. C.L.S., P.J.A.S., and A.V. acknowledge financial support from the São Paulo Research Foundation (FAPESP), grant Nos. 2019/03301-8 and 2013/10559-5. A.A.V. acknowledges funding from the European Research Council (ERC) under the European Union's Horizon 2020 research and innovation programme (grant agreement No. 817540, ASTROFLOW).

ORCID iDs

Caius L. Selhorst https://orcid.org/0000-0002-5897-5236
Cassio L. Barbosa https://orcid.org/0000-0002-4922-0552
Paulo J. A. Simões https://orcid.org/0000-0002-4819-1884
Aline A. Vidotto https://orcid.org/0000-0001-5371-2675
Adriana Valio https://orcid.org/0000-0002-1671-8370

References

Allan, A., & Vidotto, A. A. 2019, MNRAS, 490, 3760
Allart, R., Bourrier, V., Lovis, C., et al. 2019, A&A, 623, A58
Bastian, T. S., Dulk, G. A., & Leblanc, Y. 2000, ApJ, 545, 1058
Beaugé, C., & Nesvorný, D. 2013, ApJ, 763, 12
Borucki, W. J., Koch, D., & Basri, G. 2010, Sci, 327, 977
Bourrier, V., & Lecavelier des Etangs, A. 2013, A&A, 557, A124
Bourrier, V., Lecavelier des Etangs, A., Ehrenreich, D., Tanaka, Y. A., & Vidotto, A. A. 2016, A&A, 591, A121
Dewdney, P. E., Hall, P. J., Schilizzi, R. T., & Lazio, T. J. L. W. 2009, IEEEP, 97, 1482
Ehrenreich, D., Bourrier, V., Wheatley, P. J., et al. 2015, Natur, 522, 459
Farrell, W. M., Desch, M. D., & Zarka, P. 1999, JGR, 104, 14025
Fossati, L., Bagnulo, S., Elmasli, A., et al. 2010, ApJ, 720, 872
Fulton, B. J., Petigura, E. A., Howard, A. W., et al. 2017, AJ, 154, 109
Grießmeier, J. M., Zarka, P., & Spreeuw, H. 2007, A&A, 475, 359
Hallinan, G., Doyle, G., Antonova, A., et al. 2009, in AIP Conf. Ser. 1094, 15th Cambridge Workshop on Cool Stars, Stellar Systems, and the Sun, ed. E. Stempels (Melville, NY: AIP), 146
Hallinan, G., Sirothia, S. K., Antonova, A., et al. 2013, ApJ, 762, 34
Johnstone, C. P., Güdel, M., Stökl, A., et al. 2015, ApJL, 815, L12
Kao, M. M., Hallinan, G., Pineda, J. S., et al. 2016, ApJ, 818, 24
Kavanagh, R. D., Vidotto, A. A. Ó., Fionnagáin, D., et al. 2019, MNRAS, 485, 4529
Kavanagh, R. D., & Vidotto, A. A. 2020, MNRAS, 493, 1492
Kubyshkina, D., Fossati, L., Erkaev, N. V., et al. 2018, ApJL, 866, L18
Kulow, J. R., France, K., Linsky, J., & Loyd, R. O. P. 2014, ApJ, 786, 132
Lai, D., Helling, C., & van den Heuvel, E. P. J. 2010, ApJ, 721, 923
Lazio, T. J. W., & Farrell, W. M. 2007, ApJ, 668, 1182
Lecavelier des Etangs, A., Bourrier, V., Wheatley, P. J., et al. 2012, A&A, 543, L4
Lecavelier des Etangs, A., Sirothia, S. K., & Gopal-Krishna, Z. P. 2013, A&A, 552, A65
Liseau, R., de la Luz, V., O'Gorman, E., et al. 2016, A&A, 594, A109
Llama, J., Jardine, M. M., Wood, K., Hallinan, G., & Morin, J. 2018, ApJ, 854, 7
Llama, J., & Shkolnik, E. L. 2015, ApJ, 802, 41
Llama, J., & Shkolnik, E. L. 2016, ApJ, 817, 81
Matsakos, T., Uribe, A., & Königl, A. 2015, A&A, 578, A6
Mazeh, T., Holczer, T., & Faigler, S. 2016, A&A, 589, A75
Nortmann, L., Pallé, E., Salz, M., et al. 2018, Sci, 362, 1388
Oklopčić, A. 2019, ApJ, 881, 133
Pope, B. J. S., Bedell, M., Callingham, J. R., et al. 2020, ApJL, 890, L19
Pope, B. J. S., Withers, P., Callingham, J. R., & Vogt, M. F. 2019, MNRAS, 484, 648
Poppenhaeger, K., Schmitt, J. H. M. M., & Wolk, S. J. 2013, ApJ, 773, 62
Sánchez-López, A., Alonso-Floriano, F. J., López-Puertas, M., et al. 2019, A&A, 630, A53
Selhorst, C. L., Barbosa, C. L., & Válio, A. 2013, ApJL, 777, L34
Selhorst, C. L., Silva, A. V. R., & Costa, J. E. R. 2005a, A&A, 433, 365
Selhorst, C. L., Silva, A. V. R., & Costa, J. E. R. 2005b, A&A, 440, 367
Selhorst, C. L., Simões, P. J. A., Brajša, R., et al. 2019, ApJ, 871, 45
Silva, A. V. R. 2003, ApJL, 585, L147
Sirothia, S. K., Lecavelier des Etangs, A., Gopal-Krishna, Kantharia, N. G., & Ishwar-Chandra, C. H. 2014, A&A, 562, A108
Smith, A. M. S., Collier Cameron, A., Greaves, J., et al. 2009, MNRAS, 395, 335
Spake, J. J., Sing, D. K., Evans, T. M., et al. 2018, Natur, 557, 68
Tan, C., Yan, Y., Tan, B., et al. 2015, ApJ, 808, 61
Vedantham, H. K., Callingham, J. R., Shimwell, T. W., et al. 2020, NatAs, tmp, 34
Vidal-Madjar, A., Lecavelier des Etangs, A., Désert, J. M., et al. 2003, Natur, 422, 143
Vidotto, A. A., & Donati, J. F. 2017, A&A, 602, A39
Vidotto, A. A., Fares, R., Jardine, M., Moutou, C., & Donati, J. F. 2015, MNRAS, 449, 4117
Vidotto, A. A., Feeney, N., & Groh, J. H. 2019, MNRAS, 488, 633
Vidotto, A. A., Jardine, M., & Helling, C. 2010a, ApJL, 722, L168
Vidotto, A. A., Jardine, M., & Helling, C. 2011, MNRAS, 414, 1573
Vidotto, A. A., Opher, M., Jatenco-Pereira, V., & Gombosi, T. I. 2010b, ApJ, 720, 1262
Villarreal D'Angelo, C., Esquivel, A., Schneiter, M., & Sgró, M. A. 2018, MNRAS, 479, 3115
Villarreal D'Angelo, C., Schneiter, M., Costa, A., et al. 2014, MNRAS, 438, 1654
Weber, C., Lammer, H., Shaikhislamov, I. F., et al. 2017, MNRAS, 469, 3505
Wolszczan, A., & Frail, D. A. 1992, Natur, 355, 145
Zarka, P., Lazio, J., & Hallinan, G. 2015, in Advancing Astrophysics with the Square Kilometre Array (AASKA14), ed. T.L. Bourke (Trieste: SISSA), 120